ACS OMEGA

http://pubs.acs.org/journal/acsodf

Article

# Limitations of Ultrathin $Al_2O_3$ Coatings on LNMO Cathodes

Elise R. Østli,* Yonas Tesfamhret, Sigurd Wenner, Matthew J. Lacey, Daniel Brandell, Ann Mari Svensson, Sverre M. Selbach, and Nils P. Wagner*

Cite This: *ACS Omega* 2021, 6, 30644−30655

Read Online

ACCESS | Metrics & More | Article Recommendations | Supporting Information

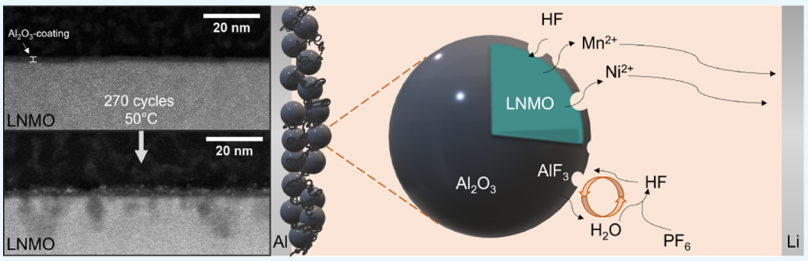


**ABSTRACT:** This study demonstrates the application of $Al_2O_3$ coatings for the high-voltage cathode material $LiNi_{0.5-x}Mn_{1.5+x}O_{4-\delta}$ (LNMO) by atomic layer deposition. The ultrathin and uniform coatings (0.6−1.7 nm) were deposited on LNMO particles and characterized by scanning transmission electron microscopy, inductively coupled plasma mass spectrometry, and X-ray photoelectron spectroscopy. Galvanostatic charge discharge cycling in half cells revealed, in contrast to many published studies, that even coatings of a thickness of 1 nm were detrimental to the cycling performance of LNMO. The complete coverage of the LNMO particles by the $Al_2O_3$ coating can form a Li-ion diffusion barrier, which leads to high overpotentials and reduced reversible capacity. Several reports on $Al_2O_3$-coated LNMO using alternative coating methods, which would lead to a less homogeneous coating, revealed the superior electrochemical properties of the $Al_2O_3$-coated LNMO, suggesting that complete coverage of the particles might in fact be a disadvantage. We show that transition metal ion dissolution during prolonged cycling at 50 °C is not hindered by the coating, resulting in Ni and Mn deposits on the Li counter electrode. The $Al_2O_3$-coated LNMO particles showed severe signs of pitting dissolution, which may be attributed to HF attack caused by side reactions between the electrolyte and the $Al_2O_3$ coating, which can lead to additional HF formation. The pitting dissolution was most severe for the thickest coating (1.7 nm). The uniform coating coverage may lead to non-uniform conduction paths for Li, where the active sites are more susceptible to HF attack. Few benefits of applications of very thin, uniform, and amorphous $Al_2O_3$ coatings could thus be verified, and the coating is not offering long-term protection from HF attack.

## ■ INTRODUCTION

Energy storage and electrification of the transport sector are critical measures for reducing global greenhouse gas emissions. Secondary batteries have been shown to be a viable solution of energy storage for consumer electronics as well as electric propulsion and stationary energy storage. For the former two applications, batteries with high energy density are of utmost importance. The best-performing battery technology to date with respect to energy density and cycle life are secondary Li-ion batteries (LiBs) where the cathode consists of a Li transition metal (TM) oxide. The use of scarce resources such as Co and Ni in the cathode is a major cost factor and has a negative impact on the environmental footprint.[1] As the fleet of electric vehicles is expected to grow immensely over the next years,[2] alternative high-energy cathode materials based on abundant materials are in urgent need. The two main factors that determine the energy density of a battery are the specific capacity of the electrode materials and their difference in the electrochemical potential. Considerable effort has been put into the development of improved, high-capacity cathode materials such as nickel-rich layered oxides, where the reversible capacity is increased by increasing the Ni content.[3,4] Another route to increase the energy density is the implementation of high-voltage cathode materials. With its notably high operating potential of 4.7 V versus $Li/Li^+$, $LiNi_{0.5-x}Mn_{1.5+x}O_{4-\delta}$ (LNMO) stands out as a promising cathode material for use in the next-generation LiBs. LNMO yields a comparable energy density to nickel-rich $LiNiMnCoO_2$ (NMC) cathodes, while the reduction in Ni content (0.16 g Ni/1 g LNMO vs 0.48 g Ni/1 g NMC811) and the absence of Co will reduce both the price and the environmental footprint of the former.[1,5] Even if the high operating potential increases

**Received:** August 17, 2021
**Accepted:** October 22, 2021
**Published:** November 3, 2021

ACS Publications

© 2021 The Authors. Published by American Chemical Society

the risk of CO and $CO_2$ evolution from electrolyte decomposition reactions, the onset potential of these reactions has been shown to be high for LNMO compared to NMC.[3,6] Still, issues concerning the unstable cathode/electrolyte interface lead to both TM dissolution and severe electrolyte degradation.[7,8] TM dissolution has been observed for several cathode materials and is thus not a problem only associated with the high operating voltage of LNMO.[9,10] The Mn-ion dissolution in the spinel $LiMn_2O_4$ (LMO) has been assigned to the disproportionation reaction ($2Mn^{3+} \rightarrow Mn^{2+} + Mn^{4+}$) and Jahn−Teller distortions.[11−13] While the $Mn^{3+}$ content in LNMO is reduced compared to that in LMO due to the partial substitution of $Mn^{3+/4+}$ by $Ni^{2+}$, synthesis conditions that induce structural disorder, oxygen deficiencies, and rocksalt-structured impurity phases (such as $Li_xNi_{1-x}O$[14]) can generate $Mn^{3+}$ in LNMO.[15,16] Disproportionation reactions and the resulting TM dissolution are thus a problem also for LNMO. The dissolved TM ions will migrate over to the anode and deposit, interfering with the insulating characteristic of the solid electrolyte interphase (SEI). Pieczonka et al.[7] observed metallic Mn and Ni particles on the graphite electrode from a 100 cycle LNMO||graphite full cell, indicating that the TM ions are reduced on the graphite surface. The following continuous formation of new SEI will consume the cyclable Li and be detrimental to the cycle life in full cells with a finite amount of cyclable Li.[17]

The commercial LiB electrolytes contain $LiPF_6$ salt in carbonate solvents such as ethylene carbonate (EC), diethyl carbonate (DEC), dimethyl carbonate, and ethyl methyl carbonate.[18] Several of the electrolyte components are not stable at the high operating voltage of LNMO. As an example, EC will polymerize on the LNMO surface to form a polyethylene carbonate film.[8] Furthermore, $LiPF_6$ hydrolyses readily with a trace amount of water forming HF and $POF_3$.[7,19−21] HF can in turn attack the LNMO material and lead to increased TM dissolution. These unfortunate effects are thus shortening the lifetime of the battery and must be resolved before LNMO-based LiBs can be fully commercialized.

Protective surface coatings have been suggested as a viable strategy to protect the LNMO surface from HF attack and prevent TM dissolution.[22−24] The chemically simple, cheap, and abundant $Al_2O_3$ has been widely investigated as a possible protective surface coating for electrodes in LiBs.[25] The relatively low ionic and electronic conductivity of most $Al_2O_3$ phases,[26] however, makes the coating thickness critical, in particular when amorphous coatings are applied. Ultrathin coatings are therefore desirable. Both Song et al.[27] and Park et al.[28] reported improved capacity retention for ultrathin atomic layer deposition (ALD) coatings of composite electrodes containing in-house synthesized LNMO. Coating of the entire electrode laminate will, in addition to protecting the active material, also protect the carbon black additive from direct contact with the electrolyte. It has been demonstrated that electrolyte degradation takes place both on the carbon black surface and on the surface of the active material at high voltages.[29] Furthermore, the surface area of carbon black has been found to be proportional to the extent of solvent oxidation and the degree of TM dissolution in the case of $LiMnO_2$ cathodes.[30] However, extracting information about the LNMO/electrolyte interface in itself is challenging based on the results from coated electrodes, as the coating is altering both the LNMO and the carbon black surface.

Kim et al.[31] reported on ultrathin $Al_2O_3$ ALD coating (<1 nm) of commercial LNMO powder and found that the coating improved the Coulombic efficiency, cycle retention, and self-discharge behavior at 30 °C to some extent. The coating, however, also increased the overpotential and reduced the obtainable capacity. This corresponds well with the findings from Jung et al.,[32] who compared $Al_2O_3$ coating of $LiCoO_2$ (LCO) particles and LCO-containing electrode and found that coating of the active material by itself introduced a larger overpotential, which was attributed to the limited electronic conductivity in the $Al_2O_3$ film resulting from complete coverage of the LCO particles. $Al_2O_3$ coatings applied by solid-state sintering were found to offer only temporary protection from HF attack.[33,34] This was attributed to the fact that $Al_2O_3$ is known to act as a HF scavenger, causing challenges with the consumption of the surface coating. Hall et al.[35] showed in addition that $Al_2O_3$ can react directly with $PF_6^-$ in the electrolyte to form $Al_2O_{3-x}F_2$ and $AlF_3$. The fluorination of $Al_2O_3$ is accompanied by a substantial volume change, something that could induce the formation of cracks in the coating and exposure of bare, unprotected LNMO surface.[31] Although improved electrochemical performance has been reported at 60 °C for $Al_2O_3$-coated NMC, for which the coating was applied by solution precipitation,[34] an important aspect is the degree of protection by the $Al_2O_3$ coating over a prolonged time. While the current commercially available LNMO materials has demonstrated significantly improved cycling stability at room temperature over the last years (78% capacity retention has been achieved after 300 cycles[36]), the cycling stability drops dramatically at higher temperatures, which hinders the practical use of the materials for a number of applications. Thus, long-term protection from HF attack by the coating, and in particular at higher temperatures, is essential to justify the use of surface coatings. Further knowledge of the extent of protection over time, particularly at more extreme conditions such as elevated temperatures, is therefore needed to understand whether such coatings are beneficial to the battery lifetime.

In view of the scattered results previously reported on $Al_2O_3$ coatings, we have in this work investigated coatings applied by ALD, a technique that allows for accurate control of the coating thickness and the possibility to produce ultrathin and uniform surface coatings.[37] Ultrathin, amorphous $Al_2O_3$ coatings were deposited on commercial LNMO and their influence on the electrochemical properties, cycling stability, and TM dissolution at higher temperatures was investigated. Three different thicknesses of $Al_2O_3$ coatings were deposited by exposing the LNMO to 5, 10, and 20 ALD cycles with trimethylaluminum (TMA) and $H_2O$ as precursors. The resulting materials were characterized by X-ray diffraction (XRD), Raman spectroscopy, scanning electron microscopy (SEM), inductively coupled plasma mass spectrometry, scanning transmission electron microscopy (STEM), and X-ray photoelectron spectroscopy (XPS) to investigate the quality of the coated materials. A systematic comparison of the electrochemical performance of the materials, with emphasis of cycling stability, was done at room temperature and at 50 °C, and TM dissolution was identified.

## ■ RESULTS AND DISCUSSION

**Materials Characterization.** Three different thicknesses of $Al_2O_3$ were deposited on the LNMO powder by exposing it to 5, 10, and 20 ALD cycles. The samples are hereafter named


https://doi.org/10.1021/acsomega.1c04457
ACS Omega 2021, 6, 30644−30655

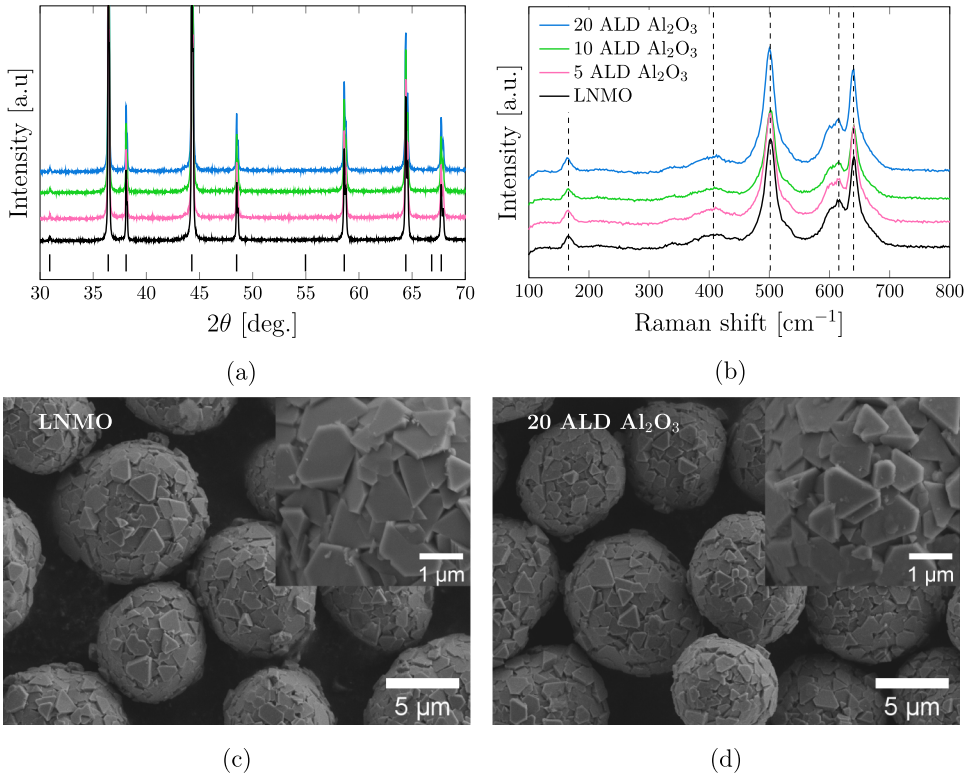


**Figure 1.** Powder XRD patterns (a) and Raman spectra (b) of pristine LNMO (black) 5 ALD $Al_2O_3$ (pink), 10 ALD $Al_2O_3$ (green), and 20 ALD $Al_2O_3$ (blue). The vertical bars in panel (a) indicate reflections for disordered LNMO with the space group $Fd\bar{3}m$ (PDF# 00-063-0626). The SEM micrographs show the morphology of the pristine LNMO powder (c) and the 20 ALD $Al_2O_3$ powder (d).

as 5 ALD $Al_2O_3$, 10 ALD $Al_2O_3$, and 20 ALD $Al_2O_3$, respectively. Due to the low deposition temperature during the ALD coating procedure (120 °C), no change in the bulk LNMO is expected. Higher deposition temperatures and/or post-deposition heating steps are interesting approaches in order to change the crystallinity of the coating layer and increase the interfacial bonding strength between the LNMO substrate and the coating layer. Interdiffusion of the coating material into the bulk is, however, a possible additional effect, and careful parameter optimization in a separate study is required.[38] From the X-ray diffractograms depicted in Figure 1a, no difference between the four LNMO powders is observed, and no introduction of new impurity phases in the coated samples is detectable. All samples display reflections, which can be indexed with the high-symmetry phase with the space group $Fd\bar{3}m$ of phase pure LNMO. This space group of LNMO is characterized by structural disorder where Mn and Ni cations are randomly positioned on the 16d sites and Li and O atoms are occupying 8a and 32e sites, respectively.[39] The Raman spectra in Figure 1b confirm that the LNMO is predominantly disordered. The peaks at around 165 and 407 $cm^{-1}$ correspond to Ni−O bands and are signatures of partial ordering in the spinel structure.[15,40,41] The peak intensities of these features are expected to increase with increased ordering of the LNMO structure. The low observed intensity indicates that the degree of ordering in these samples is low. No peak shifts can be observed for the four samples; however, some small variations in peak intensity can be seen. Raman spectrometry, with a typical probing depth of 20−300 nm,[15] is not surface sensitive enough to probe only the coating layer. These changes are thus not explained by the coating as most of the signal is coming from the LNMO bulk phase. These small variations can instead be assigned to the morphology of the particles. The morphology of the pristine LNMO and the 20 ALD $Al_2O_3$ powders are depicted in Figure 1c,d, respectively. The spherical secondary particles consist of polyhedral shaped primary particles resulting in a rough surface with many edges that can give rise to the observed intensity variations in the Raman spectra. There is no observable difference in the powder morphology of the pristine LNMO and the LNMO with the thickest $Al_2O_3$ coating (20 ALD $Al_2O_3$). Based on these results, we conclude that there is no apparent change in the bulk LNMO due to the coating procedure.

Inductively coupled plasma sector field mass spectrometry (ICP-SFMS) analysis was conducted on the uncoated and coated LNMO samples. A stoichiometry of $Li_{1.08}Ni_{0.46}Mn_{1.54}O_4$ is calculated from the measured average Li, Ni, and Mn content of all four samples, presented in Table S1, and corresponds well with the stoichiometry provided by the LNMO powder supplier ($LiNi_{0.43}Mn_{1.57}O_4$). The measured Al content, presented in Table 1, is as expected increasing with increasing number of ALD cycles applied. The coating thickness for a homogeneous coverage was estimated by using the measured BET surface area of the LNMO powder

**Table 1. Al Content as Measured by ICP-SFMS and the Calculated Coating Thickness for the Samples**

| sample name | Al content (RSD 15−25%) [mg/kg] | calculated coating thickness [nm] |
|---|---|---|
| LNMO | 10 | |
| 5 ALD $Al_2O_3$ | 239 | 0.6 |
| 10 ALD $Al_2O_3$ | 373 | 1 |
| 20 ALD $Al_2O_3$ | 661 | 1.7 |


https://doi.org/10.1021/acsomega.1c04457
ACS Omega 2021, 6, 30644−30655

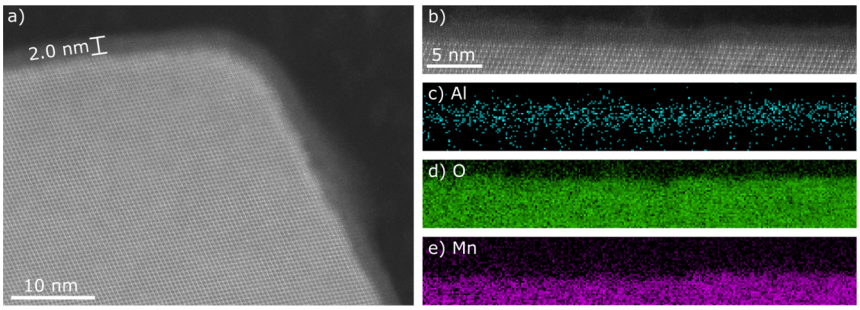


**Figure 2.** STEM results from the cross section of a 20 ALD $Al_2O_3$ particle. (a) ADF-STEM micrograph showing the uniformly thick coating over a facet corner. (b) Higher magnification ADF-STEM image of coating on a facet. (c−e) Corresponding EELS elemental maps from the Al−K, O−K, and Mn-L2,3 core loss edges, showing the presence of aluminum oxide.

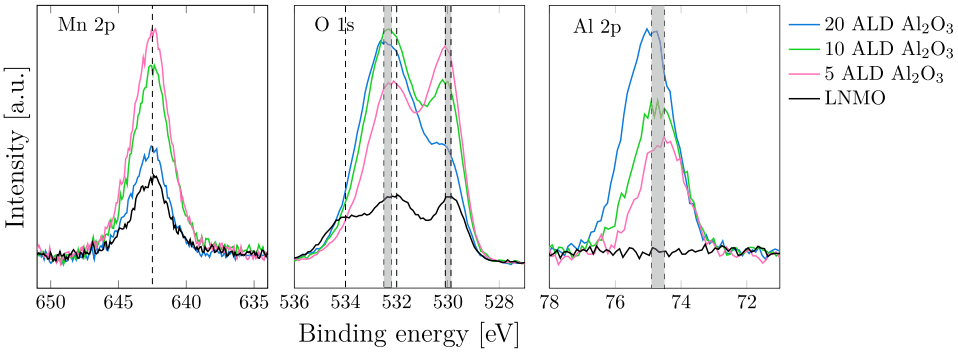


**Figure 3.** Mn 2p, O 1s, and Al 2p XPS spectra for the pristine LNMO (black), 5 ALD $Al_2O_3$ (pink), 10 ALD $Al_2O_3$ (green), and 20 ALD $Al_2O_3$ (blue).

(0.276 $m^2/g$) and the density of the amorphous $Al_2O_3$ (from the work of Groner et al.[42] estimated to be 2.7 $g/cm^3$).

The 20 ALD $Al_2O_3$ powder was analyzed by STEM coupled with electron energy loss spectroscopy (EELS). The uniformity and thickness of the coating layer are shown in Figure 2. Figure 2a shows an annular dark-field (ADF)-STEM micrograph. A uniform amorphous layer with an even thickness of approximately 2 nm is observed on the crystalline LNMO particle surface. The coating covers all the inner and outer corners between facets. The EELS elemental maps (Figure 2c−e) show that the surface layer contains Al and O. The observed coating thickness corresponds well with the findings of Cho et al.[43] who estimated the $Al_2O_3$ coating thickness after 20 ALD cycles on LNMO electrodes to be slightly lower than 2 nm when applying the coating with TMA and $H_2O$ as precursors at 250 °C. The calculated coating thickness of 20 ALD $Al_2O_3$ (1.7 nm) based on the ICP-SFMS results also correspond well to the coating thickness observed in the STEM micrograph, further confirming the homogeneity of the coating.

The surface sensitivity of XPS makes it possible to probe the outermost surface of the particles, making this a suitable technique to gain additional information about the ultrathin $Al_2O_3$ coating. Electrodes containing the four samples, carbon black, and poly(vinylidene difluoride) (PVDF) were analyzed in XPS prior to electrochemical testing. The XPS elemental spectra (Mn 2p, O 1s, and Al 2p) of the electrodes are presented in Figure 3. In order to compare the samples, all the peak intensities have been normalized with respect to the F 1s peak and energy calibrated to C 1s at 285 eV. The F 1s peak was chosen as a reference as the F content from the PVDF binder is assumed to be comparable for all the samples. The uncoated LNMO (black) shows a lower intensity in the Mn 2p and O 1s spectra compared to the $Al_2O_3$-coated samples. The calculated surface elemental concentrations (in atomic percentages) included in the Supporting Information (Table S1) show that the measured carbon content in the pristine LNMO sample (81.6 at. %) is higher than for the $Al_2O_3$-coated samples (67.6−70 at. %), while the oxygen content is lower (3.5 at. % for uncoated LNMO and 8.5−9.1 at. % for the $Al_2O_3$-coated samples). This apparent difference in the C-content could be explained by the introduction of O on the surface by the $Al_2O_3$ coating, which will dilute the C concentration originating from the surface groups (such as C═O and C−O species) present on the pristine LNMO surface. The coating procedure could also change the affinity to accumulate surface-bound carbon due to the change in surface-bound groups. As the $Al_2O_3$ growth cycle is terminated with TMA exposure, the $Al_2O_3$-coated LNMO will, to a large extent, have $-CH_3$-groups on the surface after ALD coating. Since the XPS analysis has been performed on electrodes, it cannot be excluded that the slurry process has affected the LNMO surface. The $-CH_3$ surface groups on the $Al_2O_3$-coated samples could, as an example, react with moisture/air during the slurry process and form methanol, which in turn would leave the surface. By comparing the three $Al_2O_3$-coated powders, there is a clear trend with decreasing intensity in the Mn 2p peak with increasing $Al_2O_3$ coating thickness. This is expected as the increasing $Al_2O_3$ coating thickness will, to a larger extent, shield for the Mn 2p signal.

Three distinct peaks are present in the O 1s spectra for the uncoated LNMO, while two main peaks are present for the three $Al_2O_3$-coated samples. The peak at 529.9−530.1 eV, which is present in all spectra, is assigned to the metal oxide


https://doi.org/10.1021/acsomega.1c04457
ACS Omega 2021, 6, 30644−30655

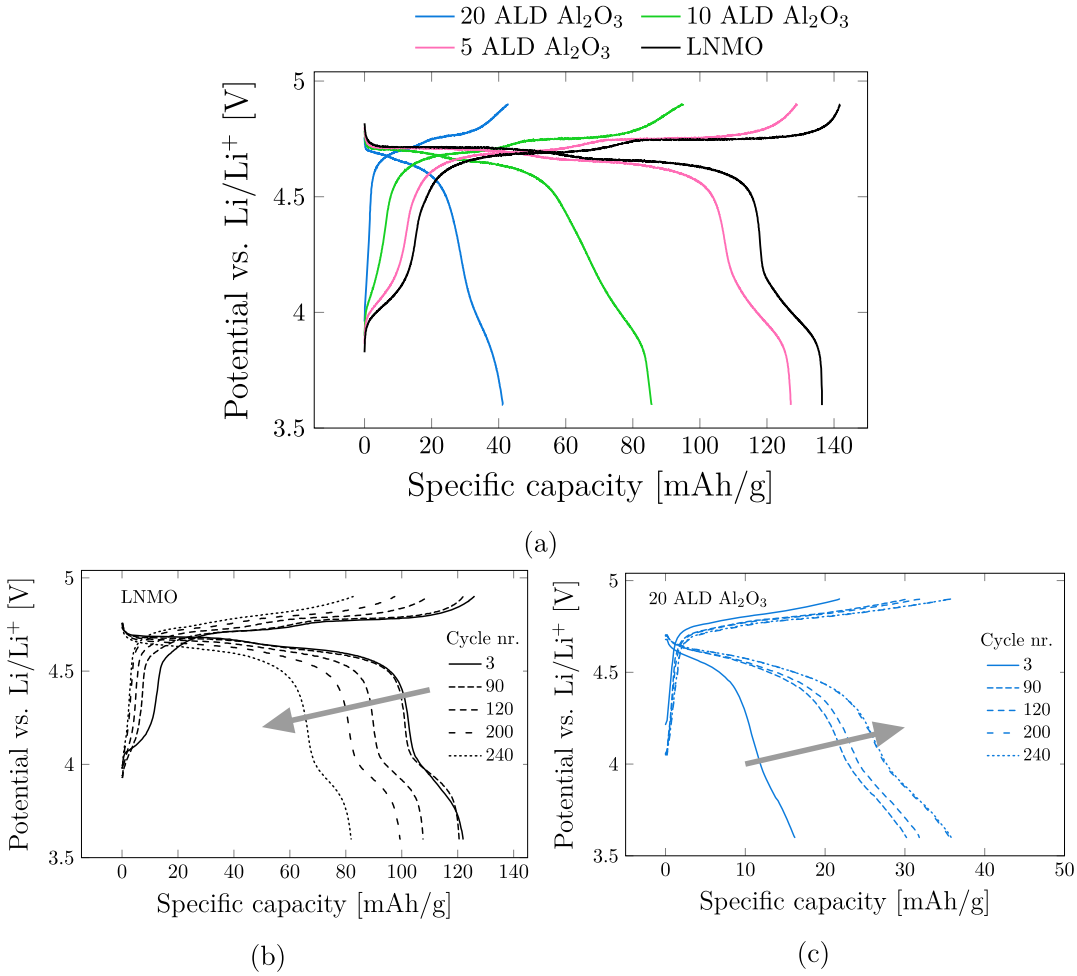


**Figure 4.** Second charge cycle at room temperature (a) for the pristine LNMO (black), 5 ALD $Al_2O_3$ (pink), 10 ALD $Al_2O_3$ (green), and 20 ALD $Al_2O_3$ (blue) at C/10. The charge−discharge curves showing the development with increasing number of cycles (indicated with arrows) for LNMO (b) and 20 ALD $Al_2O_3$ (c) with a current of C/2 for all plotted cycles.

(M−O) (M = Ni, Mn, and Al).[44−46] The peaks at 532 and 534 eV present in the uncoated LNMO spectrum are assigned to surface-bound C═O and C−O species, respectively.[46,47] For the $Al_2O_3$-coated samples, the second peak at 532.2−532.5 eV is assigned to the metal hydroxide M−OH (M = Al).[44,45] The presence of an Al−OH O 1s peak suggests that not all the Al−OH groups are replaced with Al−$CH_3$ groups by the final TMA exposure in the coating procedure or that the slurry process has altered the surface-bound groups, as mentioned earlier. The relative intensity of the M−O O 1s peak to the M−OH O 1s peak is decreasing with increasing number of ALD cycles applied.

For the uncoated LNMO (black), there is as expected no Al 2p signal, while the Al 2p signal intensity is clearly increasing with increasing ALD coating thickness (5 ALD $Al_2O_3$ < 10 ALD $Al_2O_3$ < 20 ALD $Al_2O_3$). This supports the ICP-SFMS results where an increased Al amount was found for increasing number of ALD cycles applied. It furthermore indicates that Al is on the outermost surface of the LNMO particles and that the surface coating does not seem to be damaged to a large extent by the slurry and electrode coating process. There is a slight shift to higher BE values for the Al 2p peak with increasing coating thickness (from 74.5 eV for the 5 ALD $Al_2O_3$ to 74.9 eV for the 20 ALD $Al_2O_3$). This peak shift has been attributed to residual −OH groups at the outermost surface of the coated particles.[48] It has also been suggested that amorphous structures will give rise to an Al 2p transition to a higher binding energy,[44] and this shift can thus be an indication of increasing contributions from the amorphous $Al_2O_3$ phase with increasing coating thickness.

Taken together, the results show that the ALD coating strategy is successful, rendering homogeneous $Al_2O_3$ layers that uniformly cover the LNMO particles, and where the thickness follow the number of coating cycles. The analysis does not show any indications of contaminants in the coatings. Thereby, the coatings generated should be a useful platform for studying the influence on electrochemical performance.

**Electrochemical Characterization.** The uncoated and coated LNMO powders were tested in CR-2032 coin cells with Li foil as a counter electrode. Cycling experiments were carried out both at room temperature and at 50 °C. The cells were initially cycled at C/10 between 3.6 and 4.9 V versus $Li/Li^+$ for two cycles. Thereafter, the long-term cycling stability was evaluated at C/2 in the same potential range. The voltage curves of the second charging cycle at room temperature of all the four samples are shown in Figure 4a. The uncoated LNMO shows the typical voltage curve of disordered LNMO, with the two main plateaus around 4.7 V versus $Li/Li^+$ ($Ni^{2+/4+}$ redox activity) and a smaller plateau around 4 V versus $Li/Li^+$ attributed to $Mn^{3+/4+}$ redox activity.[15] A clear effect of the


https://doi.org/10.1021/acsomega.1c04457
ACS Omega 2021, 6, 30644−30655

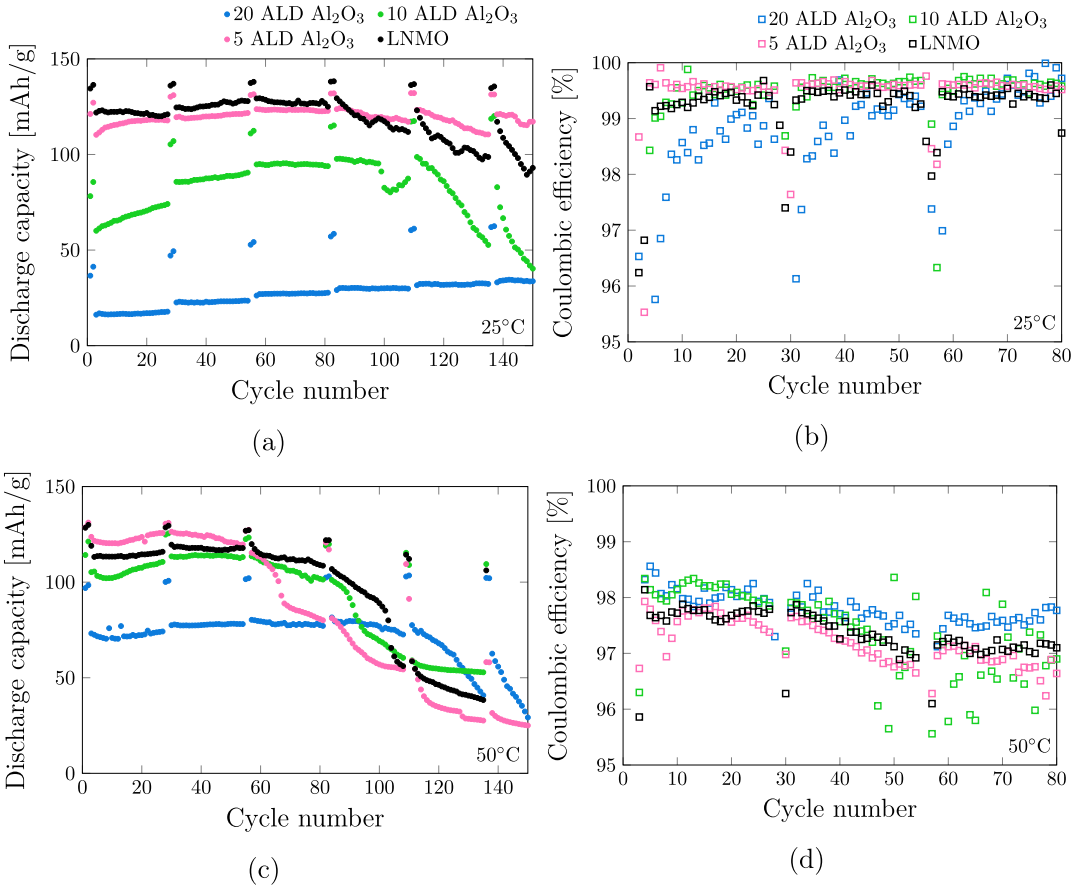


**Figure 5.** Discharge capacity and Coulombic efficiency for the cells cycled at room temperature (a,b) and the cells cycled at 50 °C (c,d) for pristine LNMO (black), 5 ALD $Al_2O_3$ (pink), 10 ALD $Al_2O_3$ (green), and 20 ALD $Al_2O_3$ (blue). The *C*-rates are *C*/2 for all cycles with two *C*/10 cycled every 25 cycles. Due to the large variation in cell behavior at 50 °C, the discharge capacity in (c) is the average value from 3 to 5 cells. The slow charging cycles (*C*/10) every 25th cycle is added to gain information about the origin of the capacity fade.

$Al_2O_3$ coating on the reversible capacity and the polarization upon charge and discharge of LNMO is visible. The pristine LNMO shows the highest reversible capacity (136 mA h/g), while the obtained capacity is reduced slightly for the 5 ALD $Al_2O_3$ to 127 mA h/g. The 10 ALD cycle coated sample showed a reversible capacity of 85 mA h/g, and in the case of 20 ALD cycle coated sample, the capacity was reduced to merely 41 mA h/g. In contrast to several other studies where wet chemical,[49] mechanochemical,[50] and pulse laser deposition[51] coating methods were applied, we found even a 2 nm thin $Al_2O_3$ coating layer to be severely detrimental to the initial reversible capacity. One possible reason for the variety in reported results is the differences in the degree of coating coverage. The $Al_2O_3$ coatings investigated in this study are very thin and uniform with continuous coverage. The ALD coatings have been deposited at 120 °C, most probably yielding a coating with a large degree of structural disorder. The Li-ion conductivity/diffusivity is expected to be very low for amorphous $Al_2O_3$ coatings.[26] This, in addition to the band gap, which has been experimentally determined to be 9.9 eV [for thin (20 nm) amorphous films deposited onto silicon wafers],[52] will make the $Al_2O_3$ coating a resistive layer that could act as a barrier for Li-ion diffusion and electronic conductivity. The complete coverage of the LNMO particles could thus be a disadvantage. A more inhomogeneous surface decoration on the other hand, which will result in more electrochemical active sites, could in fact be an advantage as it would not slow down the Li-ion diffusion to the same extent but still scavenge HF and in that way protect the active material from HF attack.

By looking at the development with increasing number of charge−discharge cycles (shown in Figure 4b,c for pristine LNMO and 20 ALD $Al_2O_3$, respectively), an opposite trend is observed for the pristine LNMO (black) and the 20 ALD $Al_2O_3$ (blue). The pristine LNMO shows increasing polarization and capacity decay with increasing number of cycles. This is expected due to decomposition products forming an interphase layer on the LNMO surface during cycling, leading to increased resistance for Li-ion diffusion. For the 20 ALD $Al_2O_3$, however, the trend is reversed. Increasing number of charging cycles results in a reduction in the polarization and increased capacity. Assuming that the $Al_2O_3$ coating is the main reason for the initial polarization, it is clear that the properties of the coating or the degree of coating coverage are changing during cycling. This is consistent with the findings of Kim et al.[31] where this increase in capacity and reduced polarization with increasing number of charging cycles was assigned to the fluorination of $Al_2O_3$ that is accompanied by a volume change of 64%, which could lead to cracking of the surface coating and exposing of bare LNMO surface. The observed increase in discharge capacity with increasing number of charging cycles for the 20 ALD $Al_2O_3$ can alternatively be explained by a more gradual consumption of the $Al_2O_3$ coating through HF scavenging, leading to a thinner and less


https://doi.org/10.1021/acsomega.1c04457
ACS Omega 2021, 6, 30644−30655

homogeneous coating layer that would allow for more facile Li-ion transport and consequently lower the polarization.

Long-term galvanostatic cycling, both at room temperature and at 50 °C, was performed. After two formation cycles at C/10, the cells were cycled at C/2 with two C/10 cycles every 25 cycles. Cycling at lower current rates can reveal whether the observed capacity decay originates from kinetic limitations or is caused by material degradation in Li excess systems such as Li metal half-cells. The discharge capacity for 150 cycles and the Coulombic efficiency at room temperature and at 50 °C are presented in Figure 5a−d. The high-temperature measurements presented in Figure 5c are average values from 3 to 5 cells as the onset of capacity decay varied. Only the first 150 cycles are presented for the measurements at 50 °C, as not all of the cells were cycled up to 270 cycles. Plots with standard deviations as error bars for the 50 °C measurements and all 270 cycles for the room temperature measurements are included in the Supporting Information (Figures S1 and S2, respectively). At room temperature, the uncoated and 5 ALD materials exhibit stable cycling up to 80 cycles at a capacity of 120 and 110 mA h/g, respectively. Afterward, capacity fading is observed at C/2, but the samples regained their initial capacity when cycled at C/10. The 10 and 20 ALD $Al_2O_3$ samples on the other hand show low initial capacities of 85 and 60 mA h/g, respectively. In contrast to the uncoated LNMO and 5 ALD $Al_2O_3$ samples, the 10 ALD and 20 ALD samples showed increasing capacity values at C/2 and C/10. The 10 ALD sample reached values of 100 mA h/g at C/10 and 120 mA h/g at C/2 after 120 cycles before this sample also began to lose capacity again. The 20 ALD showed a constant increase in capacity over 150 cycles, but even after 150 cycles, the capacity was still below 50 mA h/g. The total charge that passed through the material or the number of equivalent full cycles is hence lower and the time spent at high voltage is thus shorter for this sample, possibly resulting in reduced electrolyte decomposition and a more stable cycling. At 50 °C, a similar trend was observed, although the onset of capacity fade occurs after fewer charge−discharge cycles for all samples. For the first 60 cycles, the 5 ALD $Al_2O_3$ cycles at a higher capacity (120 mA h/g) than the uncoated LNMO (110 mA h/g), indicating a small improvement in the cycling properties at higher temperature for the 5 ALD $Al_2O_3$. The 10 and 20 ALD $Al_2O_3$ both show higher capacity at 50 °C than at room temperature before the capacity fade onset, with a capacity more similar to that of the uncoated LNMO. 10 ALD $Al_2O_3$ cycles at 100−110 mA h/g for C/2 and 120 mA h/g at C/10, while the 20 ALD $Al_2O_3$ cycles at 75 mA h/g at C/2 and 100 mA h/g at C/10. It has been found that the diffusivity of Li in $Al_2O_3$ obeys a near-ideal Arrhenius behavior,[26] and the cycling performance is consistent with significantly improved $Li^+$ transport properties through the $Al_2O_3$ coating at elevated temperatures. It should be noted that the extreme Li excess in half-cells can hide certain degradation effects, while the Li metal can introduce others. Björklund et al.[53] showed that the cross talk between the Li metal anode and the NMC cathode leads to rapid capacity fading compared to when anode materials such as graphite and $Li_4Ti_5O_{12}$ (LTO) were used. In addition, the carbon black constitutes a substantial part of the surface area of the electrode, even with just 5 wt % carbon black, and the electrolyte degradation occurs on the carbon black surface in addition to the surface of the active material at high voltages.[29] The loss of capacity can thus be due to several undesired effects, but it can be assumed that the majority of the observed capacity fading is not due to degradation of the active material as all the cells regain most of their initial capacity in the cycles with a lower C-rate. This behavior shows that the capacity loss is most likely due to kinetic limitations from, for example, electrolyte degradation. To sum up, the results clearly show that the $Al_2O_3$ coating thicker than 0.6 nm has a detrimental effect on the electrochemical properties of LNMO. It furthermore does not improve the cycling stability in half cells at 50 °C. The 20 ALD $Al_2O_3$ shows stable cycling at room temperature, but the improved cycling stability comes with the cost of high overpotentials and a severely reduced reversible capacity.

The Coulombic efficiencies at room temperature, presented in Figure 5b, are quite similar for the uncoated LNMO, 5 ALD $Al_2O_3$, and 10 ALD $Al_2O_3$, with stable values above 99% for the first 80 cycles. Only the first 80 cycles are included in the figure, as the Coulombic efficiency values vary greatly after the capacity fade onset. The 20 ALD $Al_2O_3$ has a slightly lower Coulombic efficiency between 98 and 99%. All of the samples show lower Coulombic efficiencies for a few cycles right after the lower current rate cycles (of C/10). This effect is increasing with increasing $Al_2O_3$ coating thickness and is especially visible for the 20 ALD $Al_2O_3$ where the Coulombic efficiency drops down to 96% before it stabilizes above 98% after two to three additional charging cycles. The combined low Coulombic efficiency and increase in capacity during cycling for the 20 ALD $Al_2O_3$ electrode, and to a certain degree for the 10 ALD $Al_2O_3$, can indicate surface reactions that change the properties of the $Al_2O_3$ coating. At 50 °C, as presented in Figure 5d, all the samples have lower Coulombic efficiency than at room temperature, varying between 97 and 98.5%. This is not surprising, as the temperature instability of the $LiPF_6$ salt[54] and the increased instability of the LNMO||Li system at higher temperature will lead to more unwanted side reactions for all samples and result in a lower Coulombic efficiency.

As the TM dissolution is expected to increase with increasing temperature,[7] the effect of $Al_2O_3$ coatings on the TM dissolution was investigated on cells cycled at 50 °C. Cycled LNMO cathodes were examined by SEM after 270 cycles at 50 °C. SEM micrographs are presented in Figure 6. No changes in the morphology could be discerned for the uncoated material. For the 20 ALD $Al_2O_3$, however, the primary particles have visible holes on the surface. The holes are relatively large (up to 100 nm in diameter) and extend into the active material. These holes are observed on several particles of the 20 ALD $Al_2O_3$ sample cycled at 50 °C. Neither of the electrodes cycled at room temperature had any LNMO particles with visible holes that could be observed with SEM. This also applies to the uncoated LNMO, 5 ALD $Al_2O_3$, and 10 ALD $Al_2O_3$ electrodes cycled at 50 °C. This does not exclude the presence of similar holes in these electrodes, but the extent of pitting formation is lower. The $Al_2O_3$ coating acts as a HF scavenger[33] and is thus consumed via sacrificial reactions with HF.

HF can be generated by various routes in $LiPF_6$-based carbonate electrolytes. The simple hydrolysis with trace amounts of water is well known and results in the formation of HF and $POF_3$.[19,54,55] Trace amounts of water can also react with EC forming ethylene glycol and $CO_2$.[56] The two-electron oxidation of ethylene glycol leads to the formation of glycolaldehyde and two protons, which will drive the dissociation of $PF_6^-$ into HF and $PF_5$. The combination of


https://doi.org/10.1021/acsomega.1c04457
ACS Omega 2021, 6, 30644−30655

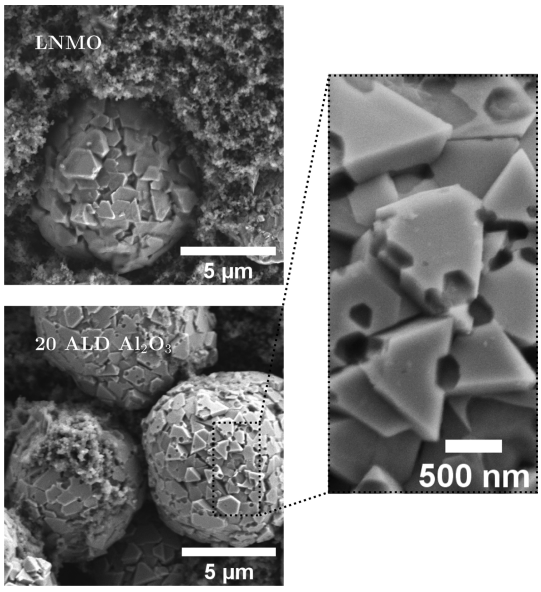


**Figure 6.** SEM micrographs showing LNMO (top) and 20 ALD $Al_2O_3$ (bottom) electrodes cycled at 50 °C for 270 cycles. Spots where the active material has been attacked are clearly visible on the 20 ALD $Al_2O_3$ particles.

high temperature and high potentials can cause yet another side reaction generating HF. Single-electron oxidation of EC forms an EC oxyradical species which will generate HF, $CO_2$, and a reactive vinyl alkoxy radical in reaction with the $PF_6^-$ anion.[57] The scavenging reactions of $Al_2O_3$ with HF generating aluminum fluoride were found by Myung et al.[34] to take place stepwise according to eqs 1−3.

$$Al_2O_3 + 2HF \rightarrow Al_2O_2F_2 + H_2O \quad (1)$$

$$Al_2O_2F_2 + 2HF \rightarrow 2Al_2OF_4 + H_2O \quad (2)$$

$$Al_2OF_4 + 2HF \rightarrow 2AlF_3 + H_2O \quad (3)$$

XPS analysis of pristine electrodes showed that Al−OH bonds are present at the surface of the $Al_2O_3$-coated LNMO samples. The presence of −OH groups on the particle surface may further increase the amount of water formed in the fluorization reaction. This is illustrated by looking at the total reaction of fluorination of $Al_2O_3$, presented in eq 4, and the fluorination of AlOOH, presented in eq 5.

$$Al_2O_3 + 6HF \rightarrow 2AlF_3 + 3H_2O \quad (4)$$

$$2AlOOH + 6HF \rightarrow 2AlF_3 + 4H_2O \quad (5)$$

The sacrificial reaction of both $Al_2O_3$ and AlOOH will generate water where the presence of hydroxy group will result in the liberation of more water than the pure oxide. The formation of water can autocatalyze $LiPF_6$ hydrolysis and hence further HF generation according to eq 6.[58]

$$LiPF_6 + H_2O \rightarrow LiF + POF_3 + 2HF \quad (6)$$

The catalytic cycle can thus lead to formation of new HF as the HF is consumed. A recent study by Tesfamhret et al.[59] demonstrated that the amount of TM ions dissolved from the spinel LMO was higher for $Al_2O_3$-coated LMO than for pristine LMO. The increase in TM dissolution was attributed to the aforementioned catalytic HF/$H_2O$ cycle, and it can be assumed that $Al_2O_3$-coated LNMO will have similar issues. The very uniform $Al_2O_3$ coating layer generated by ALD could additionally lead to non-uniform conduction paths for Li, where Li ions only travel in and out of the particle at selected and electrochemically active points where the coating is thinner or absent, in particular for thicker $Al_2O_3$ coatings. This immense reduction in electrochemically active surface area could explain the high polarization and very low reversible capacity of the 20 ALD sample. In addition, these active sites could be more susceptible to HF attack and eventually lead to the formation of the observed holes in the LNMO particles, as they cause very localized water generation leading to further HF generation. The difference between our findings and several other published works on $Al_2O_3$-coated LNMO can thus be ascribed to the high degree of coating coverage on our $Al_2O_3$-coated LNMO particles which, surprisingly, leads to a disadvantage both in regard of electrochemical properties and in the degree of protection from HF attack.

To further investigate the observed changes in the 20 ALD $Al_2O_3$ surface due to cycling at elevated temperatures, STEM analysis with EELS and energy-dispersive X-ray (EDX) spectroscopy mapping of a 20 ALD $Al_2O_3$ particle from an electrode cycled at 50 °C for 270 cycles was performed. The STEM image, depicted in Figure 7a, shows an overview of a larger faceted surface. Compared with the STEM image of the pristine 20 ALD $Al_2O_3$ particle in Figure 2, the particle surface is rougher after cycling. The even $Al_2O_3$ layer is no longer as distinct, and nano-sized holes that extend up to 20 nm into the LNMO particle are clearly visible. The holes are only a few nanometers apart and cover the majority of the particle surface. The crystal structure of LNMO is undisturbed in between the holes. This suggests that in addition to the larger holes, there is nucleation of similar sites along the whole particle surface as the material deteriorates. The ADF-STEM image depicted in Figure 7b shows the edge between the facet surface and a larger hole, similar to those visible in the lower SEM image in

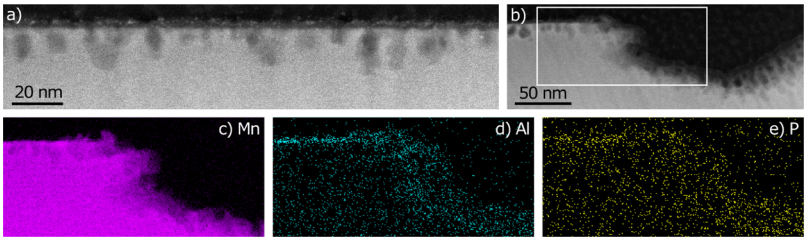


**Figure 7.** STEM results from the 20 ALD $Al_2O_3$ particle cross section. The particle is extracted from an electrode cycled at 50 °C for 270 cycles. (a) ADF-STEM image showing nano-sized holes in a faceted surface. (b) ADF-STEM image of a larger hole with corresponding (c) Mn EELS map, (d) Al EDX map, and (e) P EDX map. SEM and overview STEM images are available in the Supporting Information (Figure S3).


https://doi.org/10.1021/acsomega.1c04457
ACS Omega 2021, 6, 30644−30655

Figure 6. From the corresponding EELS and EDX maps (of Mn, Al, and P depicted in Figure 7c–e, respectively), it is clear that there is still Al present on the faceted surface after 270 charging cycles. As expected, there is a clear P signal from the surface, stemming from the $LiPF_6$ salt and decomposed electrolyte products. F could not be detected due to the overlap between the F K$\alpha$ and the Mn L$\alpha$ peaks in EDX and a similar overlap problem in EELS, where the small F K$\alpha$ peak will be hidden in the tail of the Mn L$\alpha$ due to the low F concentrations. Overall, these results further confirm that the $Al_2O_3$ coating is not sufficiently protecting the LNMO surface after prolonged cycling at 50 °C.

EDX analysis of the Li metal anode cycled against the 20 ALD $Al_2O_3$ at 50 °C for 270 cycles was performed and confirms that TM dissolution takes place in spite of the $Al_2O_3$ coating. The SEM micrograph and the EDX elemental maps are presented in Figure 8. The EDX spectra are included in the Supporting Information (Figure S4) and show that in addition to Mn, there are detectable amounts of Ni on the Li surface. In the SEM micrograph, the typical mossy structure of Li[60] can be seen in the areas not covered by a thick SEI surface film. There is a detectable amount of Mn on the Li surface that seems to correlate well with the P and F signal in the SEI film. The O signal corresponds well with the mossy Li and is most likely caused by oxidation of Li during sample transfer in air. The presence of Mn and Ni is a clear indication that the $Al_2O_3$ coating does not prevent TM dissolution when cycled at higher temperatures. Even if most batteries are not going to operate at 50 °C, locally increased temperature in larger battery packs cannot be excluded and a similar behavior at room temperature after prolonged cycling can be suspected. The clear presence of Ni and Mn on the Li counter electrode in combination with the holes in the LNMO particles (for 20 ALD $Al_2O_3$ sample) gives an indication that uniform $Al_2O_3$ coating of a certain thickness (1.7 nm) could, due to the non-uniform current distribution, cause a more severe deterioration of the LNMO-active material than for the uncoated LNMO after prolonged cycling at 50 °C. Similar changes in micro- and nanostructure cannot be excluded for the 5 and 10 ALD $Al_2O_3$ samples, but the more homogeneous current distribution for these samples will presumably make this effect less prominent.

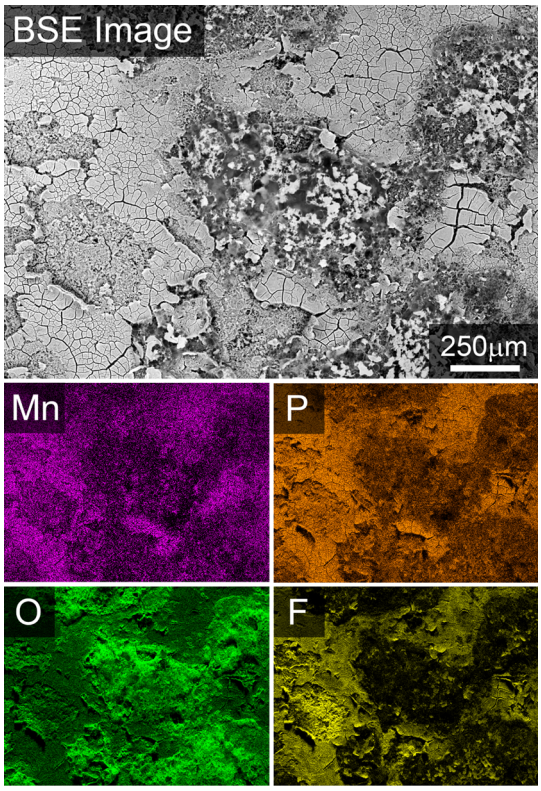


**Figure 8.** EDX image of a Li electrode cycled against 20 ALD $Al_2O_3$ at 50 °C for 270 cycles. A significant amount of Mn can be detected on all of the Li surface.

## ■ CONCLUSIONS

In this study, the long-term protection by $Al_2O_3$ coating on $LiNi_{0.5-x}Mn_{1.5+x}O_{4-\delta}$ (LNMO) has been investigated. Ultrathin $Al_2O_3$ coatings were deposited on commercial LNMO powder by ALD. With a combination of characterization techniques, a uniform coating was verified, and the coating thickness was estimated to be approximately 1.7, 1, and 0.6 nm for the 20, 10, and 5 ALD cycles, respectively. Galvanostatic charge–discharge cycling in half-cells revealed that $Al_2O_3$ coating has a negative effect on the rate capability of LNMO, and there is little observed improvement in capacity retention for the $Al_2O_3$-coated LNMO compared to uncoated LNMO both at room temperature and at 50 °C in half-cells. The high overpotential observed for the $Al_2O_3$-coated samples in this study is attributed to the homogeneity of the deposited coating, leading to a Li-ion diffusion barrier. The homogeneous coating coverage may furthermore lead to non-uniform conduction paths for Li ions, forming active sites that are more susceptible for HF attack. As the coating is consumed, the overpotential is declining with increasing number of charging cycles, and pitting holes are observed in the 20 ALD $Al_2O_3$ LNMO particles after prolonged cycling at 50 °C. This, in addition to the clear presence of Ni and Mn on the Li surface after cycling, demonstrates that the use of ultrathin and uniform $Al_2O_3$ coatings will not inhibit TM ion dissolution from the high-voltage LNMO cathode over repeated cycling, particularly at higher temperatures.

## ■ EXPERIMENTAL SECTION

LNMO with a chemical composition of $LiNi_{0.43}Mn_{1.57}O_4$ was purchased from Haldor Topsøe (Denmark). $Al_2O_3$ powder coatings were deposited in a PICOSUN R-200 Standard ALD system at 120 °C to avoid condensation. TMA (EpiValence) and $H_2O$ were used as precursors. The precursor pulse time was set to 0.2 s at a flow rate of 15 sccm and a following carrier gas purge time of 5 s at a flow rate of 100 sccm. $N_2$ was used as a carrier gas. The procedure was repeated 10 times to achieve a net of each precursor pulsing time of 2 s. The reactor was purged with carrier gas for 60 s at a flow rate of 600 sccm in between precursors. A subsequent exposure of the sample to the $H_2O$ and TMA precursors completed one growth cycle, and 5, 10, and 20 ALD growth cycles were implemented to prepare samples, named 5 ALD $Al_2O_3$, 10 ALD $Al_2O_3$, and 20 ALD $Al_2O_3$, respectively. The vacuum condition in the reaction chamber was controlled to under 10 hPa.

**Materials Characterization.** X-ray diffractograms were recorded using a D8 Focus with Cu K$\alpha$ radiation ($\lambda$ = 1.54 Å) and LynxEye SuperSpeed Detector with a 6 h collection time over a 2$\theta$ range from 10 to 120°. Raman spectroscopy was performed with a Renishaw Raman spectrometer using 532 nm


https://doi.org/10.1021/acsomega.1c04457
ACS Omega 2021, 6, 30644–30655

laser, 1200 grating, 50× lens magnification, and 0.5% laser power with a 20 s acquisition time. The lateral resolution is 1−2 μm and the probing depth is approximately 100 nm. SEM analysis of the LNMO particles was conducted on a Zeiss Ultra 55 limited edition field emission scanning electron microscope (FESEM), where the LNMO particles were connected to C-tape and analyzed with an acceleration voltage of 5 kV with a working distance of 5.5 mm and a 30 μm aperture. The BET surface area of the uncoated LNMO powder was measured using a TriStar 3000 surface area and porosity analyzer. The chemical composition of the samples was analyzed by ICP-SFMS using an ICP-SFMS Element 2 (Thermo Scientific, Bremen, Germany). For the sample preparation, coated and uncoated LNMO powders were dissolved in a mixture of hydrochloric acid, nitric acid, and hydrofluoric acid. The analysis was performed by ALS Scandinavia AB. All XPS analyses were performed using an Axis Ultra DLD X-ray photoelectron spectrometer with a monochromatic Al Kα X-ray source (10 mA, 10 kV). High-resolution regional maps were collected using 20 and 0.1 eV step size for each element. Preparations of the XPS samples were done in an Ar-filled glovebox ($O_2$ and $H_2O$ levels <0.1 ppm), and the samples were transferred inert from the glovebox to XPS. All data analysis was performed using CasaXPS software, and Shirley background subtraction was used for data evaluation. STEM was done with a JEOL ARM-200F image- and probe-corrected microscope. A voltage of 200 kV and a beam current of 80 pA were used. The convergence angle was 27 mrad, and an annular dark-field detector with an inner collection angle of 35 mrad was used. EELS was performed using a GIF Quantum spectrometer with 35 mrad collection angle and 0.5 or 1 eV dispersion. Single-frame chemical maps were acquired with 10−40 ms dwell time. Preparation of TEM specimens was done using a Helios G4 dual-beam focused ion beam (FIB)-SEM instrument. LNMO particles were covered with electron-deposited and subsequently ion-deposited carbon. The particles were lifted out, attached individually to a Cu half-grid, and thinned to electron transparency with Ga ions. The final thinning was done with 2 kV ions.

**Electrochemical Characterization.** Electrode coatings for all samples were produced by making a slurry consisting of 90 wt % LNMO, 5 wt % carbon black (Imerys C-NERGY SUPER C65), and 5 wt % Kynar Flex HFP 2801 PVDF dissolved in *N*-methyl-2-pyrrolidone solvent. To avoid damaging the $Al_2O_3$ coating and deagglomeration of the secondary LNMO particles, a gentle slurry mixing was performed using a RETSCH MM400 shaker mill with three $ZrO_2$ balls (5 mm) at 25 Hz for 20 min. The slurry was coated onto 22 μm-thick carbon-coated Al foil (SDX, Showa Denko) with a gap size of 150 μm before they were dried overnight at 60 °C. Disc-shaped electrodes (12 mm) were cut and further densified at 21.7 MPa for 3 min using a uniaxial press. Before cell assembly, the electrodes were dried at 120 °C under dynamic vacuum for 12 h before transferring to an Ar-filled glovebox ($O_2$ and $H_2O$ levels <0.1 ppm). The average LNMO loading was 5 mg/cm$^2$. CR-2032 coin cells were assembled in an Ar-filled glovebox ($O_2$ and $H_2O$ levels <0.1 ppm). A Celgard 2325 separator and Li foil (0.75 mm, Alfa Aesar) were used as the counter electrode. The electrolyte (40 μL, 1 M $LiPF_6$ in 1:1 EC/DEC from Alfa Aesar) was added by a micropipette. Galvanostatic cycling was conducted using a LAND battery testing system (CT2001A) both at room temperature and at 50 °C with *C*-rates of 0.5 C with two charge−discharge cycles of 0.1 C every 25th charge cycle. 1 C corresponds to a current of 140 mA h/g. Preparations of the SEM specimens for post-mortem analysis were performed by opening the cycled cells in an Ar-filled glovebox where the cathodes were extracted. They were then left to dry before they were removed from the glovebox in a sealed, Ar-filled container. The electrodes were exposed to air for a maximum of 30 s during sample transfer. A Zeiss Ultra 55 limited edition FESEM was used for the analysis, with a voltage of 5 kV with a working distance of 5.5 mm and a 30 μm aperture. To avoid any Mn contamination from the steel casing of coin cells for the EDX post-mortem analysis, pouch cells were prepared to cycle Li metal against the 20 ALD $Al_2O_3$ cathode at high temperatures. A double-separator layer (Celgard 2325) was used to ensure no direct contact between the 20 ALD $Al_2O_3$ and the Li metal. The pouch cells were opened in an Ar-filled glovebox ($O_2$ and $H_2O$ levels <0.1 ppm) and transported in a sealed container. The Li metal anodes were exposed to air for 5 min during sample transfer. The analysis was conducted with a Hitachi S-3400N SEM.

## ■ ASSOCIATED CONTENT

### Supporting Information

The Supporting Information is available free of charge at https://pubs.acs.org/doi/10.1021/acsomega.1c04457.

Additional ICP-MS data; calculated atomic percentages; long-term cycling data; SEM image of 20 ALD $Al_2O_3$ particle selected for FIB cross-sectioning; and elemental spectra of Li counter electrode (PDF)

## ■ AUTHOR INFORMATION


### Corresponding Authors

**Elise R. Østli** − *Department of Materials Science and Engineering, NTNU Norwegian University of Science and Technology, 7491 Trondheim, Norway*; Email: elise.r.ostli@ntnu.no

**Nils P. Wagner** − *Department of Materials Science and Engineering, NTNU Norwegian University of Science and Technology, 7491 Trondheim, Norway; Sintef Industry, 7491 Trondheim, Norway*; orcid.org/0000-0002-8014-4324; Email: nils.p.wagner@ntnu.no

### Authors

**Yonas Tesfamhret** − *Department of Chemistry−Ångström Laboratory, Uppsala University, 75121 Uppsala, Sweden*

**Sigurd Wenner** − *Sintef Industry, 7491 Trondheim, Norway*

**Matthew J. Lacey** − *Scania CV AB, 151 32 Södertälje, Sweden*

**Daniel Brandell** − *Department of Chemistry−Ångström Laboratory, Uppsala University, 75121 Uppsala, Sweden*; orcid.org/0000-0002-8019-2801

**Ann Mari Svensson** − *Department of Materials Science and Engineering, NTNU Norwegian University of Science and Technology, 7491 Trondheim, Norway*

**Sverre M. Selbach** − *Department of Materials Science and Engineering, NTNU Norwegian University of Science and Technology, 7491 Trondheim, Norway*; orcid.org/0000-0001-5838-8632

Complete contact information is available at: https://pubs.acs.org/10.1021/acsomega.1c04457


### Notes

The authors declare no competing financial interest.



https://doi.org/10.1021/acsomega.1c04457
*ACS Omega* 2021, 6, 30644−30655

## ■ ACKNOWLEDGMENTS

This work was performed within MoZEES, a Norwegian Centre for Environment Friendly Energy Research (FME), co-sponsored by the Research Council of Norway (project no. 257653) and 40 partners from research, industry, and public sector. The authors acknowledge Julian Tolchard in Sintef Industry for valuable assistance in sample preparation, characterization, and data analysis by EDX. The FIB work was done within the Norwegian Micro- and Nano-Fabrication Facility, NorFab (RCN, grant 245963/F50). The TEM work was carried out at the NORTEM (RCN, grant 197405) infrastructure at the TEM Gemini Centre, Trondheim, Norway. Furthermore, the authors acknowledge Assoc. Prof. Reza Younesi at Uppsala University for fruitful discussions and Assoc. Prof. Erik Lewin at Uppsala University for access to the ALD reactor.

## ■ REFERENCES

(1) Turcheniuk, K.; Bondarev, D.; Amatucci, G. G.; Yushin, G. Battery materials for low-cost electric transportation. *Mater. Today* **2021**, *42*, 57−72.

(2) IEA. *IEA (2020), Global EV Outlook 2020*; IEA: Paris, 2020. https://www.iea.org/reports/global-ev-outlook-2020.

(3) Jung, R.; Metzger, M.; Maglia, F.; Stinner, C.; Gasteiger, H. A. Chemical vs. Electrochemical Electrolyte Oxidation on NMC111, NMC622, NMC811, LNMO, and Conductive Carbon. *J. Phys. Chem. Lett.* **2017**, *8*, 4820−4825.

(4) Li, T.; Yuan, X.-Z.; Zhang, L.; Song, D.; Shi, K.; Bock, C. Degradation Mechanisms and Mitigation Strategies of Nickel-Rich NMC-Based Lithium-Ion Batteries. *Electrochem. Energy Rev.* **2020**, *3*, 43−80.

(5) Grey, C. P.; Tarascon, J. M. Sustainability and in situ monitoring in battery development. *Nat. Mater.* **2016**, *16*, 45−56.

(6) Jung, R.; Metzger, M.; Maglia, F.; Stinner, C.; Gasteiger, H. A. Oxygen Release and Its Effect on the Cycling Stability of $LiNi_xMn_yCo_zO_2$ (NMC) Cathode Materials for Li-Ion Batteries. *J. Electrochem. Soc.* **2017**, *164*, A1361−A1377.

(7) Pieczonka, N. P. W.; Liu, Z.; Lu, P.; Olson, K. L.; Moote, J.; Powell, B. R.; Kim, J.-H. Understanding Transition-Metal Dissolution Behavior in $LiNi_{0.5}Mn_{1.5}O_4$ High-Voltage Spinel for Lithium Ion Batteries. *J. Phys. Chem. C* **2013**, *117*, 15947−15957.

(8) Yang, L.; Ravdel, B.; Lucht, B. L. Electrolyte reactions with the surface of high voltage $LiNi_{0.5}Mn_{1.5}O_4$ cathodes for lithium-ion batteries. *Electrochem. Solid-State Lett.* **2010**, *13*, A95.

(9) Hanf, L.; Henschel, J.; Diehl, M.; Winter, M.; Nowak, S. $Mn^{2+}$ or $Mn^{3+}$? Investigating transition metal dissolution of manganese species in lithium ion battery electrolytes by capillary electrophoresis. *Electrophoresis* **2020**, *41*, 697−704.

(10) Banerjee, A.; Shilina, Y.; Ziv, B.; Ziegelbauer, J. M.; Luski, S.; Aurbach, D.; Halalay, I. C. On the oxidation state of manganese ions in li-ion battery electrolyte solutions. *J. Am. Chem. Soc.* **2017**, *139*, 1738−1741.

(11) Liu, T.; Dai, A.; Lu, J.; Yuan, Y.; Xiao, Y.; Yu, L.; Li, M.; Gim, J.; Ma, L.; Liu, J.; et al. Correlation between manganese dissolution and dynamic phase stability in spinel-based lithium-ion battery. *Nat. Commun.* **2019**, *10*, 4721.

(12) Whittingham, M. S. Lithium batteries and cathode materials. *Chem. Rev.* **2004**, *104*, 4271−4302.

(13) Hunter, J. C. Preparation of a new crystal form of manganese dioxide: λ-MnO2. *J. Solid State Chem.* **1981**, *39*, 142−147.

(14) Yi, T.-F.; Mei, J.; Zhu, Y.-R. Key strategies for enhancing the cycling stability and rate capacity of $LiNi_{0.5}Mn_{1.5}O_4$ as high-voltage cathode materials for high power lithium-ion batteries. *J. Power Sources* **2016**, *316*, 85−105.

(15) Aktekin, B.; Valvo, M.; Smith, R. I.; Sørby, M. H.; Lodi Marzano, F.; Zipprich, W.; Brandell, D.; Edström, K.; Brant, W. R. Cation Ordering and Oxygen Release in $LiNi_{0.5-x}Mn_{1.5+x}O_{4-y}$ (LNMO): In Situ Neutron Diffraction and Performance in Li Ion Full Cells. *ACS Appl. Energy Mater.* **2019**, *2*, 3323−3335.

(16) Aktekin, B.; Massel, F.; Ahmadi, M.; Valvo, M.; Hahlin, M.; Zipprich, W.; Marzano, F.; Duda, L.; Younesi, R.; Edström, K.; Brandell, D. How Mn/Ni Ordering Controls Electrochemical Performance in High-Voltage Spinel $LiNi_{0.44}Mn_{1.56}O_4$ with Fixed Oxygen Content. *ACS Appl. Energy Mater.* **2020**, *3*, 6001−6013.

(17) Kim, J.-H.; Pieczonka, N. P. W.; Li, Z.; Wu, Y.; Harris, S.; Powell, B. R. Understanding the capacity fading mechanism in $LiNi_{0.5}Mn_{1.5}O_4$ /graphite Li-ion batteries. *Electrochim. Acta* **2013**, *90*, 556−562.

(18) Schmitz, R. W.; Murmann, P.; Schmitz, R.; Müller, R.; Krämer, L.; Kasnatscheew, J.; Isken, P.; Niehoff, P.; Nowak, S.; Röschenthaler, G.-V.; et al. Investigations on novel electrolytes, solvents and SEI additives for use in lithium-ion batteries: Systematic electrochemical characterization and detailed analysis by spectroscopic methods. *Prog. Solid State Chem.* **2014**, *42*, 65−84.

(19) Heider, U.; Oesten, R.; Jungnitz, M. Challenge in manufacturing electrolyte solutions for lithium and lithium ion batteries quality control and minimizing contamination level. *J. Power Sources* **1999**, *81*−*82*, 119−122.

(20) Choi, N.-S.; Han, J.-G.; Ha, S.-Y.; Park, I.; Back, C.-K. Recent advances in the electrolytes for interfacial stability of high-voltage cathodes in lithium-ion batteries. *RSC Adv.* **2015**, *5*, 2732−2748.

(21) Tasaki, K.; Kanda, K.; Nakamura, S.; Ue, M. Decomposition of $LiPF_6$ and Stability of $PF_5$ in Li-Ion Battery Electrolytes. *J. Electrochem. Soc.* **2003**, *150*, A1628.

(22) Xu, X.; Deng, S. X.; Wang, H.; Liu, J. B.; Yan, H. Research progress in improving the cycling stability of high-voltage $LiNi_{0.5}Mn_{1.5}O_4$ cathode in lithium-ion battery. *Nanomicro. Lett.* **2017**, *9*, 22.

(23) Baggetto, L.; Dudney, N. J.; Veith, G. M. Surface chemistry of metal oxide coated lithium manganese nickel oxide thin film cathodes studied by XPS. *Electrochim. Acta* **2013**, *90*, 135−147.

(24) Liu, J.; Manthiram, A. Understanding the improvement in the electrochemical properties of surface modified 5 V $LiMn_{1.42}Ni_{0.42}Co_{0.16}O_4$ spinel cathodes in lithium-ion cells. *Chem. Mater.* **2009**, *21*, 1695−1707.

(25) Liang, G.; Peterson, V. K.; See, K. W.; Guo, Z.; Pang, W. K. Developing high-voltage spinel$LiNi_{0.5}Mn_{1.5}O_4$ cathodes for high-energy-density lithium-ion batteries: current achievements and future prospects. *J. Mater. Chem. A* **2020**, *8*, 15373−15398.

(26) Hao, S.; Wolverton, C. Lithium transport in amorphous $Al_2O_3$ and $AlF_3$ for discovery of battery coatings. *J. Phys. Chem. C* **2013**, *117*, 8009−8013.

(27) Song, J.; Han, X.; Gaskell, K. J.; Xu, K.; Lee, S. B.; Hu, L. Enhanced electrochemical stability of high-voltage $LiNi_{0.5}Mn_{1.5}O_4$ cathode by surface modification using atomic layer deposition. *J. Nanoparticle Res.* **2014**, *16*, 2745.

(28) Park, J. S.; Meng, X.; Elam, J. W.; Hao, S.; Wolverton, C.; Kim, C.; Cabana, J. Ultrathin lithium-ion conducting coatings for increased interfacial stability in high voltage lithium-ion batteries. *Chem. Mater.* **2014**, *26*, 3128−3134.

(29) Younesi, R.; Christiansen, A. S.; Scipioni, R.; Ngo, D.-T.; Simonsen, S. B.; Edström, K.; Hjelm, J.; Norby, P. Analysis of the Interphase on Carbon Black Formed in High Voltage Batteries. *J. Electrochem. Soc.* **2015**, *162*, A1289−A1296.

(30) Jang, D. H.; Oh, S. Effects of carbon additives on spinel dissolution and capacity losses in 4 V $Li/Li_xMn_2O_4$ rechargeable cells. *Electrochim. Acta* **1998**, *43*, 1023−1029.

(31) Kim, J. W.; Kim, D. H.; Oh, D. Y.; Lee, H.; Kim, J. H.; Lee, J. H.; Jung, Y. S. Surface chemistry of $LiNi_{0.5}Mn_{1.5}O_4$ particles coated by $Al_2O_3$ using atomic layer deposition for lithium-ion batteries. *J. Power Sources* **2015**, *274*, 1254−1262.

(32) Jung, Y. S.; Cavanagh, A. S.; Riley, L. A.; Kang, S.-H.; Dillon, A. C.; Groner, M. D.; George, S. M.; Lee, S.-H. Ultrathin direct atomic layer deposition on composite electrodes for highly durable and safe Li-Ion batteries. *Adv. Mater.* **2010**, *22*, 2172−2176.

(33) Ben, L.; Yu, H.; Wu, Y.; Chen, B.; Zhao, W.; Huang, X. $Ta_2O_5$ Coating as an HF Barrier for Improving the Electrochemical Cycling Performance of High-Voltage Spinel $LiNi_{0.5}Mn_{1.5}O_4$ at Elevated Temperatures. *ACS Appl. Energy Mater.* **2018**, *1*, 5589−5598.
(34) Myung, S.-T.; Izumi, K.; Komaba, S.; Sun, Y.-K.; Yashiro, H.; Kumagai, N. Role of alumina coating on Li-Ni-Co-Mn-O particles as positive electrode material for lithium-ion batteries. *Chem. Mater.* **2005**, *17*, 3695−3704.
(35) Hall, D. S.; Gauthier, R.; Eldesoky, A.; Murray, V. S.; Dahn, J. R. New Chemical Insights into the Beneficial Role of $Al_2O_3$ Cathode Coatings in Lithium-ion Cells. *ACS Appl. Mater. Interfaces* **2019**, *11*, 14095−14100.
(36) Li, W.; Cho, Y.-G.; Yao, W.; Li, Y.; Cronk, A.; Shimizu, R.; Schroeder, M. A.; Fu, Y.; Zou, F.; Battaglia, V.; Manthiram, A.; Zhang, M.; Meng, Y. S. Enabling high areal capacity for Co-free high voltage spinel materials in next-generation Li-ion batteries. *J. Power Sources* **2020**, *473*, 228579.
(37) Johnson, R. W.; Hultqvist, A.; Bent, S. F. A brief review of atomic layer deposition: From fundamentals to applications. *Mater. Today* **2014**, *17*, 236−246.
(38) Sun, P.; Ma, Y.; Zhai, T.; Li, H. High performance $LiNi_{0.5}Mn_{1.5}O_4$ cathode by Al-coating and $Al^{3+}$-doping through a physical vapor deposition method. *Electrochim. Acta* **2016**, *191*, 237−246.
(39) Cabana, J.; Casas-Cabanas, M.; Omenya, F. O.; Chernova, N. A.; Zeng, D.; Whittingham, M. S.; Grey, C. P. Composition-structure relationships in the li-ion battery electrode material $LiNi_{0.5}Mn_{1.5}O_4$. *Chem. Mater.* **2012**, *24*, 2952−2964.
(40) Boulet-Roblin, L.; Villevieille, C.; Borel, P.; Tessier, C.; Novák, P.; Ben Yahia, M. Versatile approach combining theoretical and experimental aspects of Raman spectroscopy to investigate battery materials: The case of the $LiNi_{0.5}Mn_{1.5}O_4$ spinel. *J. Phys. Chem. C* **2016**, *120*, 16377−16382.
(41) Kunduraci, M.; Amatucci, G. G. Synthesis and Characterization of Nanostructured 4.7 V $Li_xMn_{1.5}Ni_{0.5}O_4$ Spinels for High-Power Lithium-Ion Batteries. *J. Electrochem. Soc.* **2006**, *153*, A1345.
(42) Groner, M. D.; Fabreguette, F. H.; Elam, J. W.; George, S. M. Low-Temperature $Al_2O_3$ Atomic Layer Deposition. *Chem. Mater.* **2004**, *16*, 639−645.
(43) Cho, H.-m.; Chen, M. V.; Macrae, A. C.; Meng, Y. S. Effect of Surface Modification on Nano-Structured $LiNi_{0.5}Mn_{1.5}O_4$ Spinel Materials. *ACS Appl. Mater. Interfaces* **2015**, *7*, 16231−16239.
(44) Kloprogge, J. T.; Duong, L. V.; Wood, B. J.; Frost, R. L. XPS study of the major minerals in bauxite: Gibbsite, bayerite and (pseudo-)boehmite. *J. Colloid Interface Sci.* **2006**, *296*, 572−576.
(45) Iatsunskyi, I.; Kempiński, M.; Jancelewicz, M.; Załęski, K.; Jurga, S.; Smyntyna, V. Structural and XPS characterization of ALD $Al_2O_3$ coated porous silicon. *Vacuum* **2015**, *113*, 52−58.
(46) Aktekin, B.; Lacey, M. J.; Nordh, T.; Younesi, R.; Tengstedt, C.; Zipprich, W.; Brandell, D.; Edström, K. Understanding the Capacity Loss in LiNi0.5Mn1.5O4−Li4Ti5O12 Lithium-Ion Cells at Ambient and Elevated Temperatures. *J. Phys. Chem. C* **2018**, *122*, 11234.
(47) Lu, D.; Xu, M.; Zhou, L.; Garsuch, A.; Lucht, B. L. Failure Mechanism of Graphite/$LiNi_{0.5}Mn_{1.5}O_4$ Cells at High Voltage and Elevated Temperature. *J. Electrochem. Soc.* **2013**, *160*, A3138−A3143.
(48) Zhu, W.; Huang, X.; Liu, T.; Xie, Z.; Wang, Y.; Tian, K.; Bu, L.; Wang, H.; Gao, L.; Zhao, J. Ultrathin $Al_2O_3$ coating on $LiNi_{0.8}Co_{0.1}Mn_{0.1}O_2$ cathode material for enhanced cycleability at extended voltage ranges. *Coatings* **2019**, *9*, 92.
(49) Chang, Q.; Wei, A.; Li, W.; Bai, X.; Zhang, L.; He, R.; Liu, Z. Structural and electrochemical characteristics of $Al_2O_3$-modified $LiNi_{0.5}Mn_{1.5}O_4$ cathode materials for lithium-ion batteries. *Ceram. Int.* **2019**, *45*, 5100−5110.
(50) Cho, S.; Kim, S.; Kim, W.; Kim, S. Study on Electrochemical Performance of Various Oxides-Coated $LiNi_{0.5}Mn_{1.5}O_4$ Cathode for Lithium Ion Battery. *Electron. Mater. Lett.* **2019**, *15*, 481−492.
(51) Wang, Y.; Peng, Q.; Yang, G.; Yang, Z.; Zhang, L.; Long, H.; Huang, Y.; Lu, P. High-stability 5 V spinel $LiNi_{0.5}Mn_{1.5}O_4$ sputtered thin film electrodes by modifying with aluminium oxide. *Electrochim. Acta* **2014**, *136*, 450−456.
(52) Katiyar, P.; Jin, C.; Narayan, R. J. Electrical properties of amorphous aluminum oxide thin films. *Acta Mater.* **2005**, *53*, 2617−2622.
(53) Björklund, E.; Brandell, D.; Hahlin, M.; Edström, K.; Younesi, R. How the Negative Electrode Influences Interfacial and Electrochemical Properties of $LiNi_{1/3}Co_{1/3}Mn_{1/3}O_2$ Cathodes in Li-Ion Batteries. *J. Electrochem. Soc.* **2017**, *164*, A3054−A3059.
(54) Kalhoff, J.; Eshetu, G. G.; Bresser, D.; Passerini, S. Safer electrolytes for lithium-ion batteries: State of the art and perspectives. *ChemSusChem* **2015**, *8*, 2154−2175.
(55) Edström, K.; Gustafsson, T.; Thomas, J. O. The cathode-electrolyte interface in the Li-ion battery. *Electrochim. Acta* **2004**, *50*, 397−403.
(56) Kitz, P. G.; Novák, P.; Berg, E. J. Influence of Water Contamination on the SEI Formation in Li-Ion Cells: An Operando EQCM-D Study. *ACS Appl. Mater. Interfaces* **2020**, *12*, 15934−15942.
(57) Solchenbach, S.; Metzger, M.; Egawa, M.; Beyer, H.; Gasteiger, H. A. Quantification of $PF_5$ and $POF_3$ from Side Reactions of $LiPF_6$ in Li-Ion Batteries. *J. Electrochem. Soc.* **2018**, *165*, A3022−A3028.
(58) Lux, S. F.; Lucas, I. T.; Pollak, E.; Passerini, S.; Winter, M.; Kostecki, R. The mechanism of HF formation in $LiPF_6$ based organic carbonate electrolytes. *Electrochem. Commun.* **2012**, *14*, 47−50.
(59) Tesfamhret, Y.; Liu, H.; Chai, Z.; Berg, E.; Younesi, R. On the manganese dissolution process from $LiMn_2O_4$ cathode materials. *ChemElectroChem* **2021**, *8*, 1516−1523.
(60) Liu, J.; Bao, Z.; Cui, Y.; Dufek, E. J.; Goodenough, J. B.; Khalifah, P.; Li, Q.; Liaw, B. Y.; Liu, P.; Manthiram, A.; et al. Pathways for practical high-energy long-cycling lithium metal batteries. *Nat. Energy* **2019**, *4*, 180−186.


https://doi.org/10.1021/acsomega.1c04457
*ACS Omega* 2021, 6, 30644−30655